PNAS RESEARCH ARTICLE | BIOCHEMISTRY CHEMISTRY

Self-assembling dendrimer nanosystems for specific fluorine magnetic resonance imaging and effective theranostic treatment of tumors

Zhenbin Lyu[a,b,1], Brigino Ralahy[a,1], Teodora-Adriana Perles-Barbacaru[c,1], Ling Ding[a,c,1], Yifan Jiang[a], Baoping Lian[d], Tom Roussel[a], Xi Liu[a,e], Christina Galanakou[a], Erik Laurini[f], Aura Tintaru[b], Suzanne Giorgio[a], Sabrina Pricl[f,g], Xiaoxuan Liu[d], Monique Bernard[c], Juan Iovanna[e], Angèle Viola[c], and Ling Peng[a,2]

Affiliations are included on p. 9.

Edited by Jonathan Sessler, The University of Texas at Austin, Austin, TX; received December 20, 2023; accepted May 13, 2024

Fluorine magnetic resonance imaging (^{19}F-MRI) is particularly promising for biomedical applications owing to the absence of fluorine in most biological systems. However, its use has been limited by the lack of safe and water-soluble imaging agents with high fluorine contents and suitable relaxation properties. We report innovative ^{19}F-MRI agents based on supramolecular dendrimers self-assembled by an amphiphilic dendrimer composed of a hydrophobic alkyl chain and a hydrophilic dendron. Specifically, this amphiphilic dendrimer bears multiple negatively charged terminals with high fluorine content, which effectively prevented intra- and intermolecular aggregation of fluorinated entities via electrostatic repulsion. This permitted high fluorine nuclei mobility alongside good water solubility with favorable relaxation properties for use in ^{19}F-MRI. Importantly, the self-assembling ^{19}F-MRI agent was able to encapsulate the near-infrared fluorescence (NIRF) agent DiR and the anticancer drug paclitaxel for multimodal ^{19}F-MRI and NIRF imaging of and theranostics for pancreatic cancer, a deadly disease for which there remains no adequate early detection method or efficacious treatment. The ^{19}F-MRI and multimodal ^{19}F-MRI and NIRF imaging studies on human pancreatic cancer xenografts in mice confirmed the capability of both imaging modalities to specifically image the tumors and demonstrated the efficacy of the theranostic agent in cancer treatment, largely outperforming the clinical anticancer drug paclitaxel. Consequently, these dendrimer nanosystems constitute promising ^{19}F-MRI agents for effective cancer management. This study offers a broad avenue to the construction of ^{19}F-MRI agents and theranostics, exploiting self-assembling supramolecular dendrimer chemistry.

dendrimer | self-assembly | MRI | theranostics | multimodal imaging

Proton magnetic resonance imaging (^{1}H-MRI) is one of the most widely used biomedical imaging techniques (1, 2). It provides anatomic, functional, and metabolic information at high spatial resolution yet with unlimited tissue penetration. In clinical ^{1}H-MRI, contrast agents can be administered to enhance the image contrast in a number of applications (3). However, identifying differences in contrast between diseased tissues and surrounding tissues can remain challenging in ^{1}H-MRI, as H_2O constitutes over 70% of the body weight. Interest in using fluorine MRI (^{19}F-MRI) with fluorinated imaging agents is increasing (4–6) because fluorine is absent in most biological systems, and using exogenous ^{19}F-MRI agents provides background-free images with high specificity that complement with ^{1}H-MRI.

Current ^{19}F-MRI is limited to detecting ^{19}F-MRI signals when the fluorine concentration is low. ^{19}F-MRI agents with high contents of chemically equivalent fluorine nuclei need to be employed to generate sharp and intense ^{19}F-MRI signals to overcome this limitation (4–6). However, compounds with high fluorine contents are both hydrophobic and lipophobic, leading to heavy aggregation and poor solubility in water, thereby hampering the mobility of ^{19}F nuclei and attenuating the ^{19}F-MRI signal (6–8). The fluorine nuclei mobility and content as well as water solubility of a ^{19}F-MRI agent therefore need to be delicately balanced. Various ^{19}F-MRI agents have been explored (4–6), including perfluorocarbon nanoemulsions (9–11), agents with hyperbranched or dendritic architecture (12–19), and functional fluorinated groups (20–23). However, all such agents had limitations such as low signal-to-noise ratio (SNR), low fluorine content, instability, or insolubility in water.

We have recently developed modular and adaptive self-assembling dendrimer nanosystems composed of amphiphilic dendrimers for the sensitive and specific detection of cancer (24–27). These nanosystems exploit the cooperative multivalency of dendrimers alongside passive tumor targeting via the enhanced permeability and retention (EPR) effect (28–31)

Significance

Bioimaging plays an important role in diagnosing and treating disease. We constructed innovative agents for fluorine magnetic resonance imaging (^{19}F-MRI), an emerging imaging modality to complement the widely used ^{1}H-MRI by adding specificity. These ^{19}F-MRI agents are based on an amphiphilic dendrimer bearing negatively charged fluorinated terminals, enabling high fluorine contents yet without fluorine–fluorine aggregation, leading to excellent relaxation characteristics and good water solubility for use in ^{19}F-MRI. Importantly, this self-assembling ^{19}F-MRI agent could also encapsulate fluorescence dye and anticancer drug enabling ^{19}F-MRI-based multimodal imaging and theranostics in cancer detection and treatment. This study demonstrates the strong potential for modular self-assembling dendrimers in the construction of imaging and theranostic agents for biomedical applications.

The authors declare no competing interest.

This article is a PNAS Direct Submission.

[1] Z.L., B.R., T.-A.P.-B., and L.D. contributed equally to this work.

[2] To whom correspondence may be addressed. Email: ling.peng@univ-amu.fr.

This article contains supporting information online at https://www.pnas.org/lookup/suppl/doi:10.1073/pnas.2322403121/-/DCSupplemental.

for effective tumor detection. Amphiphilic dendrimers combine the self-assembling abilities of amphiphiles with dendritic structures, hence readily forming nanomicellar systems (32–34). The high structural symmetry and multivalency of the dendritic scaffold make them ideal platforms for constructing ^{19}F-MRI agents. Indeed, fluorinated moieties can be introduced at the terminals to achieve the required high content of chemically equivalent fluorine nuclei for sharp ^{19}F-MRI signals (Fig. 1). In addition, the supramolecular dendrimer nanomicelles can be loaded with hydrophobic imaging agents and drug candidates to allow ^{19}F-MRI-based multimodal imaging and theranostics (Fig. 1*A*).

In this study, we designed and synthesized amphiphilic dendrimers **1a**, **1b,** and **1c** with negatively charged fluorinated entities at the dendrimer terminals (Fig. 1*B*) for use as innovative agents for ^{19}F-MRI. These amphiphilic dendrimers harbor evenly distributed CF_3 moieties with adjacent carboxylate groups at the terminals. The negatively charged carboxylate terminals not only increase the water solubility but also generate strong charge–charge repulsion, preventing the CF_3 groups from aggregation and hence maintaining fluorine nuclei mobility for generating strong ^{19}F-MRI signals. Specifically, **1c** is nontoxic and self-assembled into supramolecular dendrimer nanomicelles with favorable properties for use in ^{19}F-MRI. The hydrophobic core of the supramolecular dendrimer formed by **1c** was further loaded with the near-infrared fluorescent (NIRF) dye DiR and the anticancer drug paclitaxel (PTX). Encapsulation of these hydrophobic agents inside the supramolecular dendrimer core had negligible impact on the relaxation properties of ^{19}F nuclei on the surface because the core was segregated in space from the surface. This enabled effective multimodal ^{19}F-MRI and NIRF imaging and ^{19}F-MRI-based theranostics for simultaneous detection and treatment of cancer. These results highlight the potential of self-assembling supramolecular dendrimers in the construction of imaging agents for biomedical ^{19}F-MRI applications.

Results and Discussion

Robust and Reliable Synthesis of Fluorinated Dendrimers. We first synthesized the fluorinated amphiphilic dendrimers **1a**, **1b**, and **1c** starting with the ester-terminated dendrimers **2a**, **2b,** and **2c**, respectively (Fig. 2*A*). **2a–c** were prepared using previously

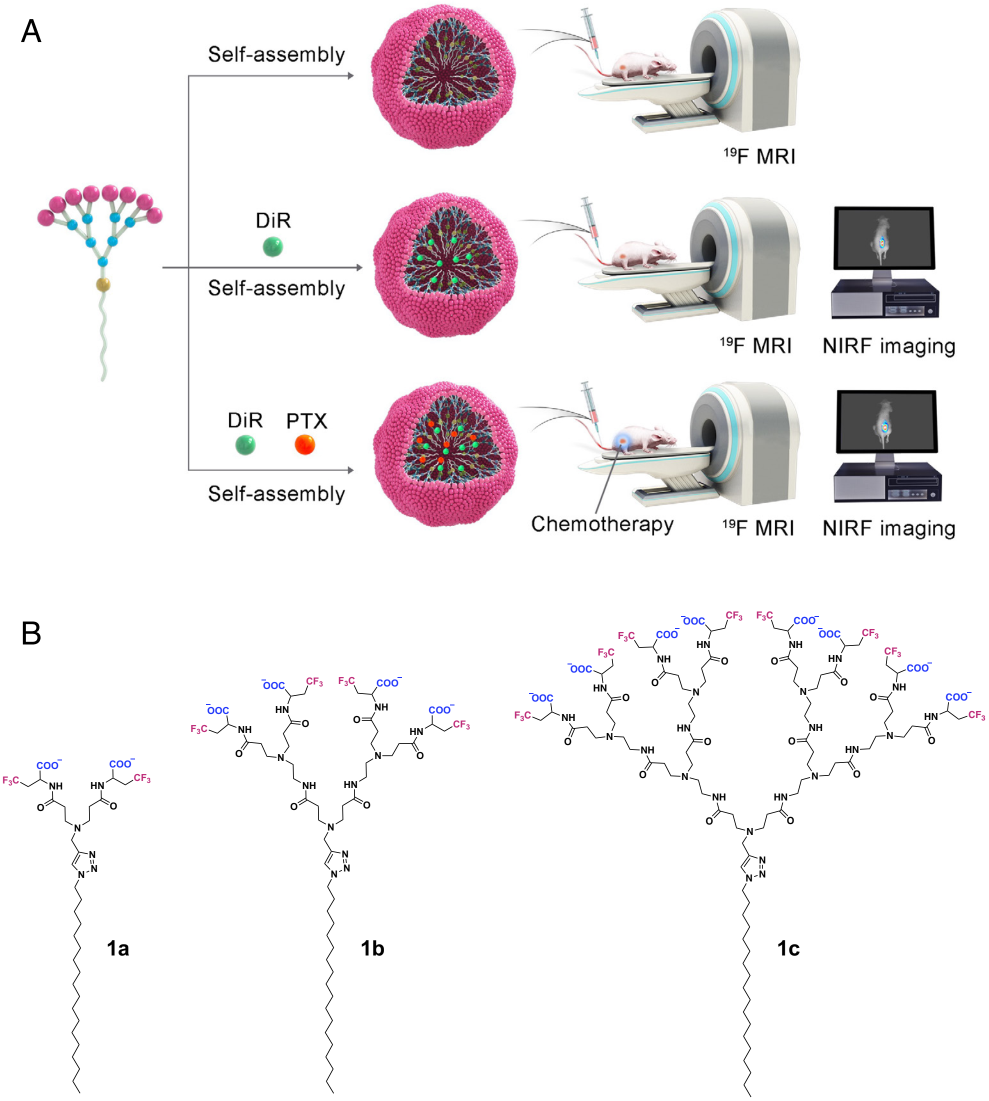

Fig. 1. Schematic illustration of self-assembling supramolecular dendrimer nanosystems for fluorine MRI (^{19}F-MRI), ^{19}F-MRI-based multimodal imaging, and theranostics. (*A*) Self-assembly of a fluorinated amphiphilic dendrimer into nanomicelles in the absence and/or presence of the NIRF probe DiR and the anticancer drug PTX within the supramolecular dendrimer core for ^{19}F-MRI, bimodal ^{19}F-MRI and NIRF imaging as well as ^{19}F-MRI-based theranostics for cancer detection and treatment. (*B*) Chemical structures of the amphiphilic dendrimers **1a–c** designed and studied for ^{19}F-MRI.

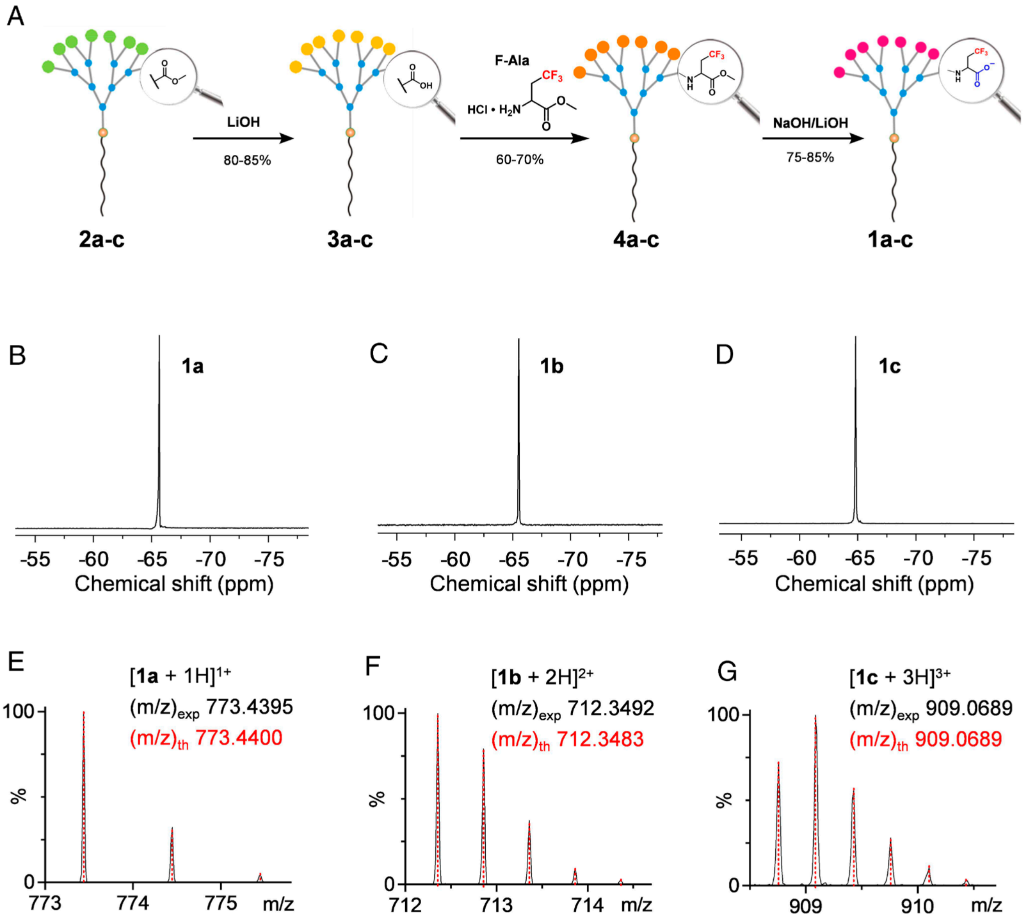

Fig. 2. Synthesis and characterization of the fluorinated amphiphilic dendrimers **1a–c**. (*A*) Synthesis scheme for **1a**, **1b**, and **1c** starting with ester-terminating dendrimers **2a**, **2b**, and **2c**, respectively. (*B–D*) Fluorine NMR (^{19}F-NMR) spectra and (*E–G*) molecular peaks in HRMS of **1a**, **1b**, and **1c**.

published methods (35), and were then hydrolyzed (36) to give the carboxylic-acid-terminating dendrimers **3a–c**. Coupling **3a–c** with the fluorinated building block **F-Ala** (a fluorinated derivative of alanine) gave **4a–c**, which were then hydrolyzed to give the target dendrimers **1a–c** (Fig. 2*A* and *SI Appendix*, Fig. S1). This robust synthesis readily gave gram-scale quantities of **1c**.

The synthesized **1a**-**c** were examined and characterized using ^{1}H-, ^{19}F-, ^{13}C-NMR analysis and high-resolution mass spectroscopy (HRMS) for their structural integrity and compositional purity (Fig. 2 *B–G* and *SI Appendix*, Fig. S2). As expected, **1a–c** gave sharp and intense characteristic singlet ^{19}F-NMR peaks (Fig. 2 *B–D*). Specifically, **1c** contains 24 chemically equivalent fluorine nuclei and has a fluorine content of 16.7% by weight, which is higher than that of many ^{19}F-MRI agents reported in the literature (4–6). Remarkably, the high fluorine content did not compromise the solubility of **1c**, which readily dissolved in water to give a clear solution, even at a concentration of 85 mg/mL. The exceptional solubility of **1c** can be mainly ascribed to the presence of negatively charged carboxylate terminals, which significantly enhance the water solubility of **1c** while preventing aggregation of the fluorinated entities via electrostatic repulsion.

Dendrimer 1c Is Nontoxic Despite Having a High Fluorine Content. Prior to any biomedical study, the safety profile of the employed agent needs assessing, particularly ^{19}F-MRI agents due to the high concentrations that are often required. We therefore first assessed the cytotoxicity of **1a–c** on various cell lines (human kidney cells HEK293, murine fibroblast cells L929, and murine ovarian cells CHO-K1) using the PrestoBlue test and the lactate dehydrogenase (LDH) assay. The PrestoBlue test measures cell viability associated with cellular metabolic activity, whereas the LDH assay evaluates cell death related to membrane damage as measured by LDH release. At concentrations up to 1.0 mM, **1c** showed no metabolic toxicity or membrane damage in any of the tested cells (Fig. 3 *A* and *B*), in contrast to **1a** which was highly toxic at concentrations above 0.25 mM and **1b** showing marked toxicity in HEK293 at a concentration of 0.50 mM (Fig. 3*A*). This discrepancy in toxicity may be due to the stronger hydrophobicity of the lower generation dendrimers leading to a higher affinity toward the cell membranes. The cell membranes would thereby destabilize more readily with the lower generation dendrimers, hence their higher cytotoxicity compared to the higher generation dendrimers.

The cytotoxicity of **1a** and **1b** led to us focusing our further studies only on **1c**. We then assessed the hemolytic toxicity of **1c**. The hemolysis assay using mouse red blood cells revealed that **1c** had very low hemolytic activity (~10%), even at 1.0 mM (*SI Appendix*, Fig. S3*A*). This result is in line with those obtained using LDH assay, as might be expected since both hemolysis and LDH assays measure cytotoxicity related to cell membrane integrity upon treatment with **1c**.

We next assessed the toxicity of **1c** in vivo by evaluating the inflammatory response and blood biochemistry, as well as histological analysis of major organs in healthy mice (Fig. 3 *C–E*). Our results show that **1c** induced no significant inflammatory response: The levels of the inflammatory factors IL-1β, IL-6, TNF-α, and INF-γ were similar to those found in the negative control group of mice treated with PBS buffer (Fig. 3*C*); mice in the positive

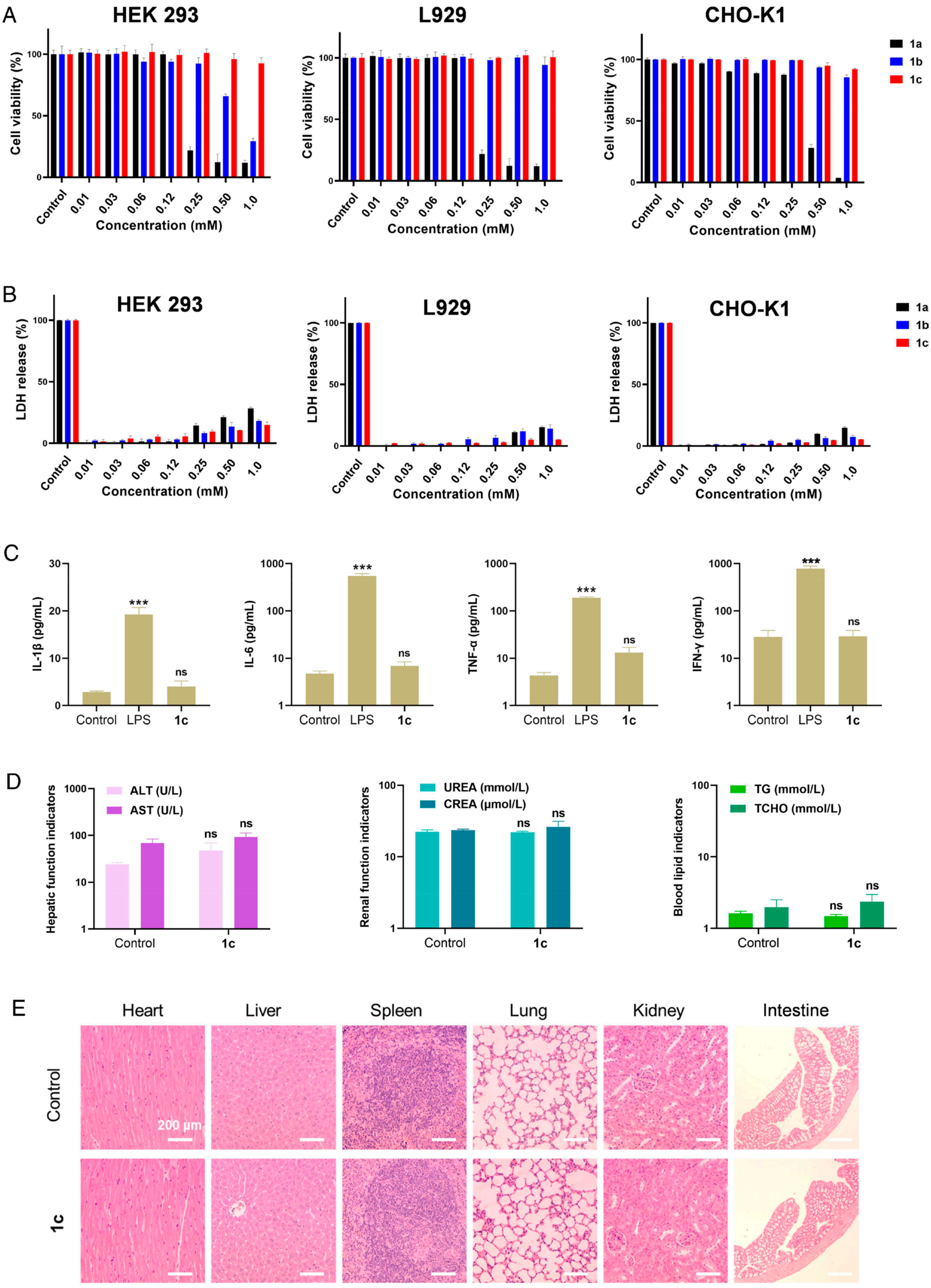

Fig. 3. Toxicity and safety evaluation of **1a–c**. (*A*) Cytotoxicity evaluation of **1a–c** on human kidney cells HEK293, murine fibroblast cells L929, and Chinese Hamster ovary cells CHO-K1 using the PrestoBlue assay. A nontreatment was used as the control. (*B*) Evaluation of membrane damage by **1a–c** on HEK293, L929, and CHO-K1 cells using the LDH release assay. A nontreatment was used as a negative control, and lysis buffer was used as a positive control for the LDH assay. Each result represents the mean ± SD (n = 3). (*C–E*) In vivo safety evaluation results for healthy mice treated with **1c**. Mice were intravenously administered **1c** (286.5 mg/kg) or PBS (control) or intraperitoneally administered LPS (5.0 mg/kg) as a positive control. (*C*) Concentrations of the inflammatory cytokines IL-1β, IL-6, TNF-α, and INF-γ in the mouse serum samples. (*D*) Liver and kidney function results. Alanine transaminase (ALT), aspartate transaminase (AST), urea, creatinine (CREA), triglyceride (TG), and total cholesterol (TCHO) concentrations in mouse serum. Each result represents the mean ± SD (n = 3). Statistical significance was calculated using two-tailed Student's *t* test and one-way ANOVA with Tukey's multiple comparison test. (ns = not significant, ****P* ≤ 0.001, vs. PBS control). (*E*) Histology of the main organs using hematoxylin and eosin staining. (Scale bar, 200 μm.)

control group treated with lipopolysaccharide (LPS) on the other hand showed significantly increased levels of IL-1β, IL-6, TNF-α, and INF-γ (Fig. 3*C*).

Major blood biochemical markers [alanine transaminase (ALT), aspartate transaminase (AST), urea, creatinine (CREA), triacylglycerol (TG), and total cholesterol (TCHO)] remained normal (Fig. 3*D*) following **1c** administration, indicating normal functioning of the major organs (including the liver and kidneys) and underlining good biocompatibility of **1c**. Histological analysis of the major organs revealed no pathological changes either (Fig. 3*E*). The lack of cytotoxic effects, inflammatory responses, and signs of pathology in major organs highlights the good safety profile for **1c**.

Self-Assembly of 1c into Nanomicelles with Favorable Relaxation Properties for ^{19}F-MRI. The amphiphilicity enabled **1c** to spontaneously self-assemble into nanoparticles (referred as to **1c@** hereafter) in water, as confirmed by dynamic light scattering (DLS) analysis (Fig. 4*A*). The transmission electron microscopy (TEM) image of **1c@** (Fig. 4*B*) confirmed the presence of small, uniform, spherical particles measuring ~25 nm in size consistent with the typical characteristics of nanomicelles. Further fluorescence spectroscopic analysis revealed a critical micelle concentration (CMC) of ~120 μM (Fig. 4*C*). The self-assembling process of the amphiphilic dendrimer **1c** into the nanoparticle **1c@** was also investigated using a rigorously validated methodology rooted in isothermal titration calorimetry (ITC) technique (37, 38). The ITC experiments (Fig. 4 *D* and *E*) yielded a CMC of 153 μM, a value consistent with the data obtained using fluorescence spectroscopy. Thermodynamic analysis of the demicellization process indicated predominantly exothermic signals upon injection of concentrated **1c** solution into water, while the reverse micellization process exhibited a corresponding positive (endothermic) micellization enthalpy value (ΔH_{mic} = +1.46 ± 0.16 kcal/mol), deduced from the integrated demicellization data fit as the difference between final and initial heat in the titration curve (Fig. 4*E*). Moreover, the use of the ITC protocol enabled the determination of the aggregation number (N_{agg}) for **1c@** as 48 ± 2.

To substantiate the spontaneous aggregation of **1c** into **1c@**, extensive atomistic molecular dynamics (AMD) simulations spanning 500 ns were conducted. Starting from a randomized distribution of 48 molecules of **1c** in solution, the AMD simulations yielded a stable **1c@** nanoassembly, as visually depicted in Fig. 4*F*. The resulting average micelle gyration radius (R_g**1c@**) was calculated as 9.0 ± 0.2 nm (Fig. 4*G*), consistent with the dimensional assessments obtained using DLS and TEM methodologies. Furthermore, a detailed examination of the conformational characteristics of the formed **1c@** nano-assemblies, along with the radial distribution analysis of the CF_3 terminal groups, unveiled the absence of backfolding and the optimal positioning of all CF_3 moieties at the micellar periphery (Fig. 4*G*).

Indeed, the ^{19}F-NMR peak of **1c@** remained remarkably sharp and intense even at 3.0 mM **1c** (>>CMC) in an aqueous solution (Fig. 4*H*), with the peak line width (full-width at half-maximum, FWHM) of 23 Hz, similar to that obtained in organic solvent (38 Hz) (Fig. 2*D*). This finding indicated the chemical equivalence and high mobility of all the fluorine nuclei in **1c@**, thus confirming fulfillment of our design concept and aim for ^{19}F-MRI.

Further evaluation of **1c@** using an MRI scanner at 7T revealed favorable T_1 and T_2 relaxation time constants (Fig. 4*I*). A short spin–lattice relaxation time constant (T_1) allows a short ^{19}F-MRI acquisition time, whereas a long spin–spin relaxation time constant (T_2) prevents rapid signal decay, meaning the ^{19}F-MRI signal can be readily acquired with MRI sequences using conventional readout trajectories (4). The T_1 values for **1c@** at fluorine concentrations of 2.50 to 20.0 mM were in the range of 534 to 593 ms, which were comparable to T_1 values for the most often used ^{19}F-MRI agents (4–6). Remarkably, the T_2 values for **1c@** at various concentrations were in the range of 192 to 426 ms, which are all above 190 ms and much higher than the T_2 values for the most commonly used ^{19}F-MRI agents (4–6). The high T_2 values confirmed the high mobility of the fluorine nuclei in **1c@** supported by our design concept using charged terminals to create strong electrostatic repulsion, thereby preventing aggregation of neighboring fluorinated moieties.

The excellent T_2 relaxation time constants of **1c@** prompted us to perform phantom studies to assess the ^{19}F-MRI performance (Fig. 4*J*). We detected a weak but measurable signal even at 0.104 mM **1c** (2.50 mM fluorine) with an acquisition time of 30 min, considered acceptable for in vivo imaging in clinical settings. Importantly, the ^{19}F-MRI signal intensity was directly proportional to **1c** concentration (Fig. 4*K*), facilitating quantitative analysis.

The promising ^{19}F-MRI properties and safety profile of **1c@** encouraged us to perform in vivo ^{19}F-MRI of cancer as a proof-of-concept study. We chose as our model the most deadly form of cancer–pancreatic cancer–for which there is still no efficacious treatment or early diagnosis imaging modality (39–41). The most effective treatment remains surgical ablation, however, the tumor boundaries for small lesions or metastases (tumor diameter <2.0 cm) are currently difficult to determine by ^{1}H-MRI (41). The development of different noninvasive imaging modalities that allow specific tumor detection would help overcome this obstacle and is of paramount importance for pancreatic cancer.

In this study, we used a tumor xenograft mouse model issued from the primary pancreatic cancer L-IPC cells (24, 42). **1c@** was administered intravenously at **1c** concentrations of 0.208 and 0.104 mmol/kg, corresponding to fluorine doses of 5.00 and 2.50 mmol/kg, respectively. Both dendrimer doses gave ^{19}F-MRI signals that colocalized with the tumors on ^{1}H-MRI (Fig. 4 *L* and *M*). We detected no ^{19}F-MRI signals in tissues surrounding the tumor, confirming the tumor-specific localization permitted by ^{19}F-MRI with **1c@**. This specificity for tumor detection can be ascribed to the unique dendritic multivalency of **1c@** and the nanosize allowing effective accumulation within the tumor lesions via the EPR effect. This phenomenon, caused by leaky vasculature and dysfunctional lymphatic drainage within the tumor microenvironment, permitted an increased accumulation and local concentration of **1c** in disease lesion and thereby effective imaging and detection of the tumor. Noteworthy is the heterogeneous distribution of ^{19}F-MRI hot-spot signals within the tumor tissue, which can be attributed to the particular heterogeneity of pancreatic cancer tumors with rich stroma and a heterogenous vascular supply (43).

It should be mentioned that no mice treated with **1c@** exhibited any abnormal behavior or signs of major organ pathology (*SI Appendix*, Fig. S3*B*). These results corroborated well with those following administration of **1c@** to healthy mice (Fig. 3*E*).

^{19}F-MRI-Based Multimodal Imaging. Incorporating multiple imaging modalities into one nanosystem offers the advantage of providing complementary imaging information favoring a more sensitive and accurate diagnosis. Combining MRI, possessing high resolution with no penetration limitation, with fluorescence imaging (44–45) offering high sensitivity but limited penetration depth, would provide powerful bimodality imaging for cancer detection. We therefore encapsulated the near-infrared fluorescent dye DiR within the supramolecular dendrimer formed by **1c** for bimodal ^{19}F-MRI and NIRF imaging. Using the film dispersion method (27), the resulting nanoparticles DiR/**1c@** were small (Fig. 5*A*), having size around 31 nm, which is comparable to **1c@**

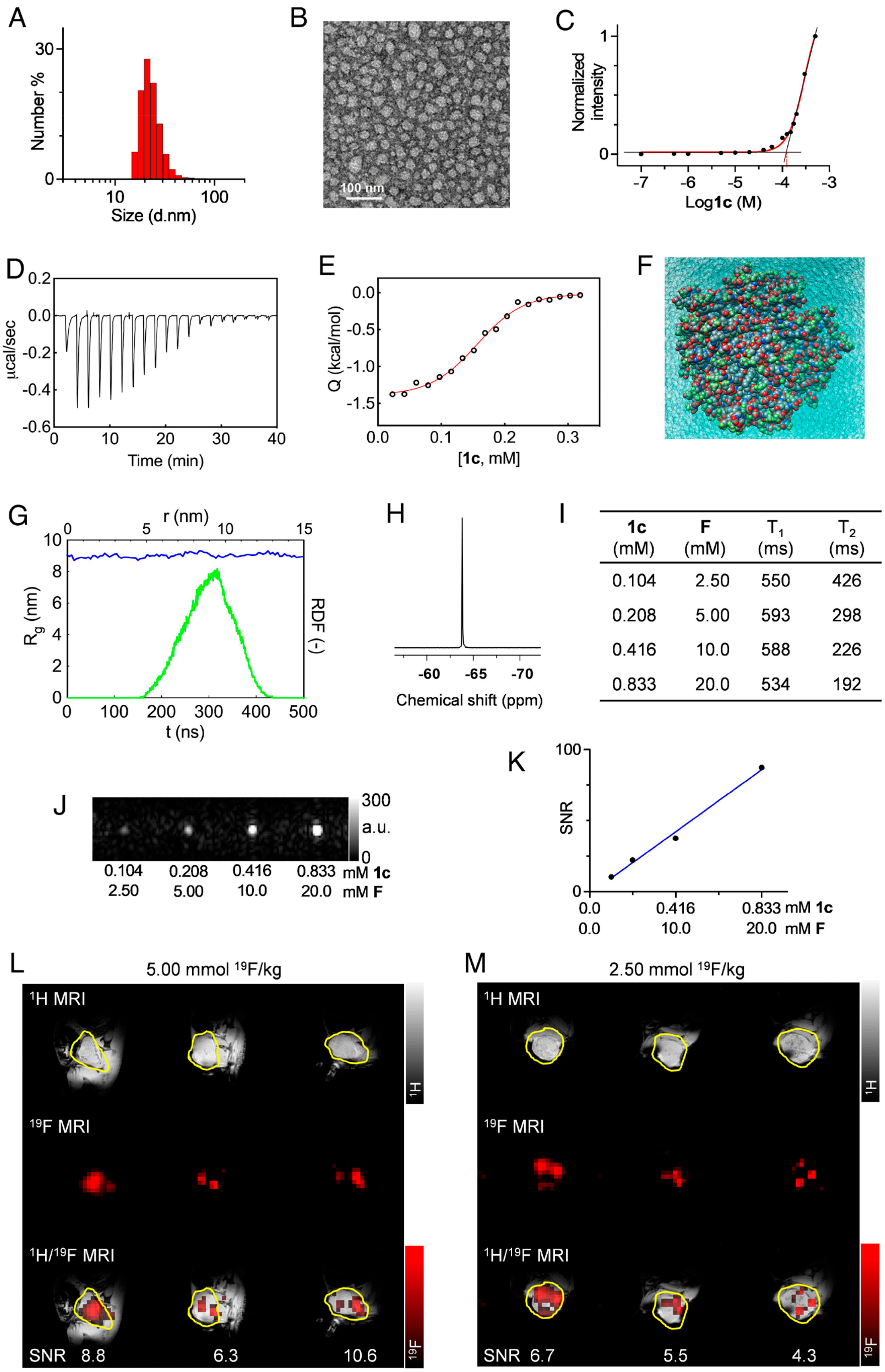

Fig. 4. Self-assembling of the amphiphilic dendrimer **1c** into nanomicelles **1c**@ for use as an imaging agent for fluorine MRI (^{19}F-MRI). (*A*) DLS results and (*B*) TEM image of the self-assembled **1c**@ nanomicelles. (*C*) CMC of **1c** estimated using a fluorescence spectroscopic assay with Nile Red. (*D*) ITC raw thermogram as obtained for the **1c**@ demicellization process. (*E*) Representative ITC profiles for the demicellization process of **1c**@ in water. The solid red line is a data fitting with a sigmoidal function. (*F*) Zoomed snapshot from the equilibrated AMD trajectory of **1c**@ (C, gray; N, blue; O, red; F, light green). Water molecules are shown as transparent aqua spheres, while all hydrogen atoms have been omitted for clarity. (*G*) Average radius of gyration (R_g) of **1c**@ as a function of time t (left *y* axis, blue curve) and radial distribution function (RDF) of the CF_3 terminals as a function of the distance r from the center of mass of **1c**@ (right *y* axis, green curve) during the equilibrated AMD trajectory. (*H*) ^{19}F-NMR spectrum of **1c**@ (3.0 mM **1c** in D_2O) recorded with a 400 MHz NMR spectrometer (376 MHz for ^{19}F) at 25 °C. (*I*) ^{19}F magnetic resonance relaxation time constants (T_1 and T_2) for **1c**@ at a magnetic field strength of 7 T and 20 °C. (*J*) In vitro ^{19}F-MR images and (*K*) ^{19}F-MRI SNR of **1c**@ at four different concentrations of **1c** and fluorine. (*L* and *M*) In vivo ^{1}H-MR anatomical images (*Top*), ^{19}F-MR images (*Middle*), and overlay of ^{1}H-MR and ^{19}F-MR images (*Bottom*) of tumors in L-IPC xenograft mice 24 h after intravenous injection of **1c**@ at **1c** concentrations of (*L*) 0.208 mmol/kg and (*M*) 0.104 mmol/kg (corresponding to fluorine concentrations of 5.00 and 2.50 mmol/kg, respectively). MR images were acquired in the sagittal plane with respect to the mouse.

(Fig. 4*B*). This can be ascribed to the effective encapsulation of DiR within the supramolecular dendrimer core.

DiR/**1c**@ retained the characteristic fluorescence of DiR (Fig. 5*B*) as shown with free DiR in an organic solvent (*SI Appendix*, Fig. S4). DiR/**1c**@ also showed similar relaxation time constants (Fig. 5*C* and *SI Appendix*, Table S2) and ^{19}F-MRI properties to **1c**@ (Fig. 5*D*). Similar to with **1c**@ (Fig. 4 *F* and *G*), the ^{19}F-MRI signal intensity increased linearly as the fluorine concentration increased with DiR/**1c**@ (Fig. 5 *D* and *E*). These results indicate that DiR/**1c**@ neither altered the NIRF properties of DiR nor the ^{19}F-MRI properties of **1c**. This can be ascribed to the fact that DiR is encapsulated within the hydrophobic inner core, whereas the fluorinated groups are on the hydrophilic outer surface of DiR/**1c**@. The two imaging modalities are thus sufficiently segregated in space to prevent their interference. The retained fluorine mobility and relaxation properties of **1c**@ with fluorescence properties of DiR hence accomplished the prerequisites for DiR/**1c**@ to be used for multimodal ^{19}F-MRI and NIRF imaging.

We therefore tested the in vivo performance of DiR/**1c**@ for multimodality MRI and NIRF imaging. ^{19}F-MRI hot-spot signals detectable in L-IPC xenograft mice treated with DiR/**1c**@ colocalized with tumors on anatomical ^{1}H-MR images (Fig. 5*F*). These results support the effective tumor imaging achieved using ^{19}F-MRI with DiR/**1c**@. We then performed NIRF imaging on the same mice having undergone ^{19}F-MRI. Tumor sites in mice treated with DiR/**1c**@ showed strong and intense fluorescence signals, in line with the ^{19}F-MRI results, whereas control mice treated with either PBS or DiR showed no detectable fluorescence signals (Fig. 5*G*). These results demonstrate the effectiveness of DiR/**1c**@ as a multimodal ^{19}F-MRI and NIRF imaging agent for tumor detection.

^{19}F-MRI-Based Theranostics for Treating Cancer. Theranostics, integrating therapeutic and diagnostic capacities in the same nanosystem, offers great promise for precision cancer treatment (46, 47). It promotes personalized medicine by enabling the individual monitoring of treatment effect and response in real time to ensure therapeutic efficacy. We investigated the potential use of **1c** in theranostics by encapsulating the anticancer drug PTX within the supramolecular dendrimer core using the film dispersion method (48, 49). We also encapsulated the near-infrared fluorescence (NIRF) dye DiR within the PTX/**1c**@ to enable the detection of tumors using multimodal MRI and NIRF imaging. The so-obtained PTX/DiR/**1c**@ showed high drug loading (23%) and produced a sharp and intense singlet ^{19}F-NMR signal (*SI Appendix*, Fig. S5). It was of similar size (33 nm) and morphology (Fig. 6*A*) to **1c**@ and DiR/**1c**@, and displayed similar NIRF (*SI Appendix*, Fig. S6) and ^{19}F-MRI properties (*SI Appendix*, Table S2 and Fig. 6 *B* and *C*). Importantly also, PTX/DiR/**1c**@ and PTX/**1c**@ produced similar T_2 values to **1c**@ (*SI Appendix*, Table S2), indicating a lack of effect of PTX encapsulation on the mobility of the fluorine nuclei on the dendrimer surface. The high drug loading and the retained favorable relaxation properties made PTX/DiR/**1c**@ particularly appealing for use in ^{19}F-MRI-based multimodality imaging and theranostics.

We performed multimodal imaging for cancer detection and assessed the theranostics capacity of PTX/DiR/**1c**@ using

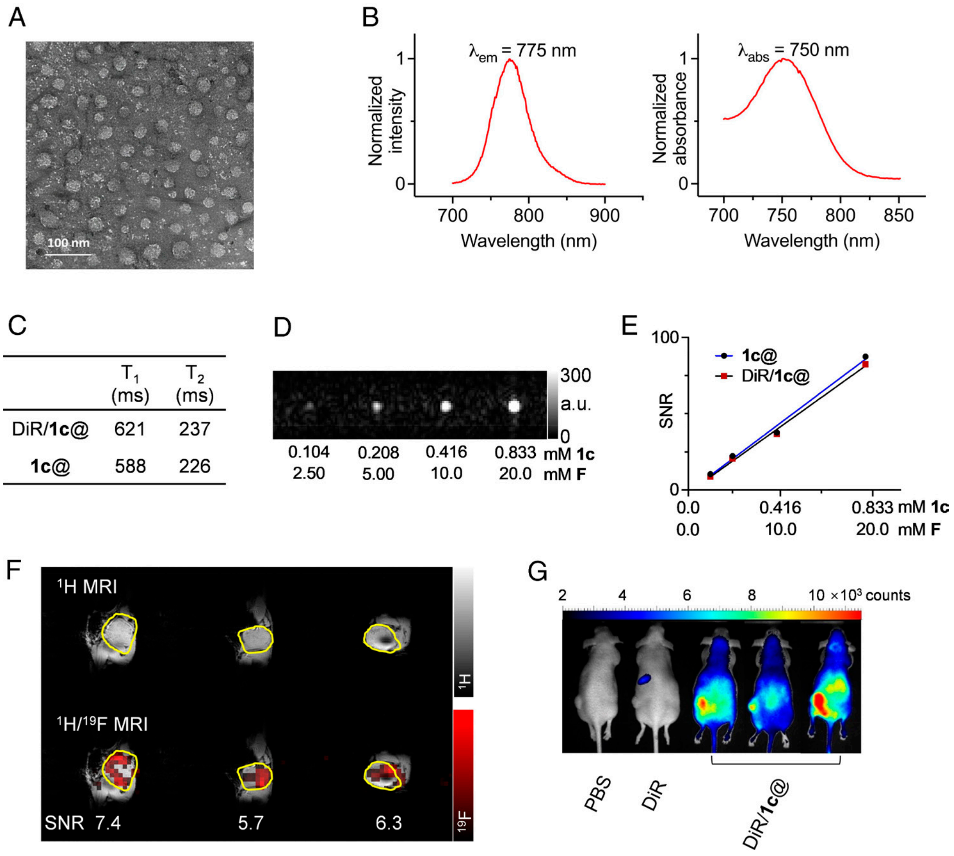

	T_1 (ms)	T_2 (ms)
DiR/**1c**@	621	237
1c@	588	226

Fig. 5. Nanoprobe DiR/**1c**@ for detecting tumors using multimodal fluorine MRI (^{19}F-MRI) and NIRF imaging. (*A*) TEM image of DiR/**1c**@. (*B*) Normalized absorbance (*Right*) and fluorescence emission (*Left*) spectra of DiR/**1c**@. (*C*) ^{19}F magnetic resonance relaxation time constants (T_1 and T_2) for DiR/**1c**@ compared to **1c**@ at a magnetic field strength of 7 T, 20 °C and 10 mM fluorine. (*D*) ^{19}F-MRI of DiR/**1c**@ at different concentrations of **1c** and fluorine. (*E*) ^{19}F-MRI SNR at 7T for **1c**@ and DiR/**1c**@ at various concentrations of **1c** and fluorine. (*F*) In vivo ^{1}H-MRI (*Top*) and ^{19}F-MRI superimposed on ^{1}H-MRI (*Bottom*) of tumors in three different L-IPC xenograft mice 24 h after intravenous injection of DiR/**1c**@. (*G*) Fluorescence images in L-IPC xenograft mice 24 h after intravenous injection of PBS, DiR, and DiR/**1c**@ [DiR: 80 μg/kg, (*F*): 5.00 mmol/kg]. MR images were acquired in the sagittal plane with respect to the mouse.

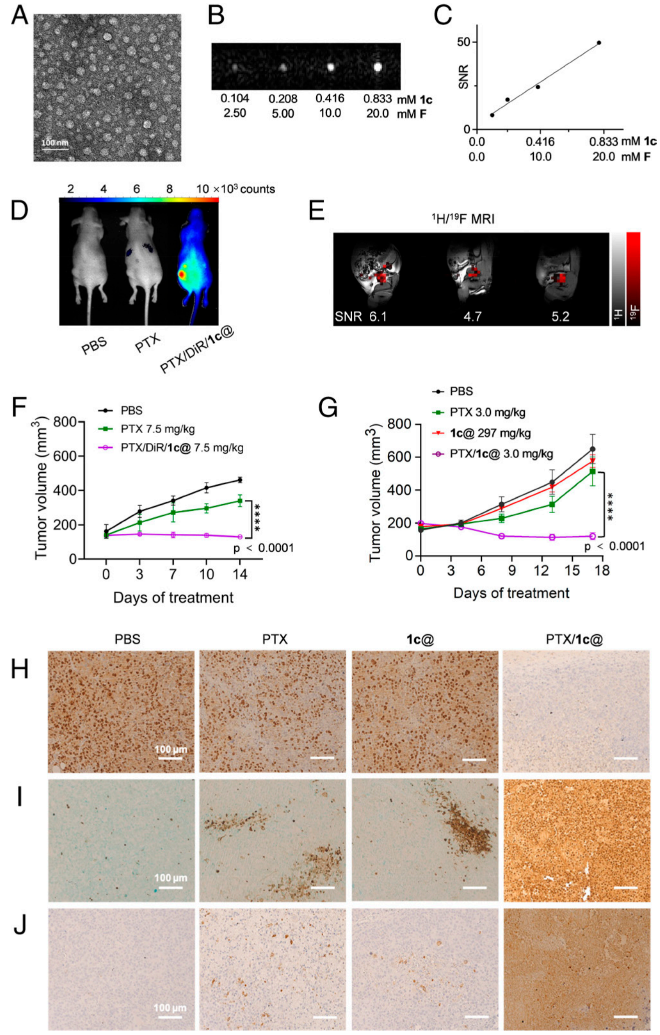

Fig. 6. PTX delivered in PTX/DiR/**1c**@ and PTX/**1c**@ nanoprobes for ^{19}F-MRI-based multimodal imaging and theranostics for tumor detection and treatment. (*A*) Transmission electron microscopic image of PTX/DiR/**1c**@. (*B*) Fluorine MRI (^{19}F-MRI) of PTX/DiR/**1c**@ at 7 T at various concentrations of **1c** and fluorine. (*C*) ^{19}F-MRI SNR of PTX/DiR/**1c**@ increasing linearly as the concentrations of **1c** and fluorine increases. (*D*) Fluorescence imaging 48 h after the first injection. (*E*) ^{19}F-MRI superimposed on anatomic ^{1}H-MRI of tumors in three different L-IPC xenograft mice 48 h after the last injection of PTX/DiR/**1c**@. Intravenous injection of PTX/DiR/**1c**@ (DiR: 80 μg/kg; **1c**: 0.21 mmol/kg; PTX: 7.5 mg/kg) twice per week for 2 wk. MR images were acquired in the sagittal plane with respect to the mouse. (*F* and *G*) Tumor growth inhibition in L-IPC xenograft mice following intravenous injection of (*F*) PTX/DiR/**1c**@ at a PTX concentration of 7.5 mg/kg (n = 3 per group) or (*G*) PTX/**1c**@ at a PTX concentration of 3.0 mg/kg (n = 5 per group) twice per week for 2 wk. Statistical differences were assessed using two-way ANOVA with Tukey's multiple comparison test. ****$P \leq 0.0001$. (*H*) Ki-67, (*I*) TUNEL assay, and (*J*) Cleaved caspase-3 immunohistochemistry staining analysis results for tumor sections from mice treated with PBS, PTX (3.0 mg/kg), **1c**@ (**1c**: 0.21 mmol/kg), and PTX/**1c**@ (PTX: 3.0 mg/kg; **1c**: 0.21 mmol/kg). (Scale bar, 100 μm.)

L-IPC-xenograft mice. Specifically, we intravenously injected PTX/DiR/**1c**@ into L-IPC-xenograft mice on days 0, 4, 7, and 11 at the PTX equivalent dose of 7.5 mg/kg. NIRF imaging indicated the presence of PTX/DiR/**1c**@ at the tumor sites (Fig. 6*D*) on day 2. ^{19}F-MRI signals were also observed in the tumors (Fig. 6*E*), confirming the performance of PTX/DiR/**1c**@ as a dual ^{19}F-MRI and NIRF imaging agent. Furthermore, mice treated with PTX/DiR/**1c**@ showed markedly inhibited tumor growth, compared to a nonsignificant inhibition in those treated with the equivalent dose of PTX only (Fig. 6*F*). Effective anticancer activity was further confirmed using PTX/**1c**@ at an even lower PTX dose of 3.0 mg/kg (Fig. 6*G*). The superior anticancer activities of both PTX/**1c**@ and PTX/DiR/**1c**@ over the free drug PTX can be ascribed to the EPR-based passive tumor targeting that is permitted through encapsulation of the drug within the nanoparticles. The resulting increased accumulation and local concentration of drug within the tumor achieves better and more efficacious treatment.

To investigate the mechanism involved in the observed inhibition of tumor growth, we used Ki-67 staining, TUNEL, and Caspase-3 activation assays to, respectively, assess cancer cell proliferation, apoptosis induction, and caspase activation in tumor tissue following treatment with PTX/**1c**@. Tumor tissues from mice treated with PTX/**1c**@ displayed considerably fewer Ki-67 positive cells (Fig. 6*H*) but many more TUNEL positive cells (Fig. 6*I*) and activated caspase-3 positive cells (Fig. 6*J*) compared to those treated with the PBS control, PTX alone, or **1c**@ alone. These results offer compelling evidence in favor of PTX/**1c**@ providing an effective antiproliferative tumor-suppressing effect in vivo brought about by the induction of caspase-dependent apoptosis.

It is important to note that all mice tolerated the treatment well and showed no detectable side effect. None displayed any abnormal behavior or marked change in body weight (*SI Appendix*, Fig. S7) throughout the treatment period, nor any pathological signs in the main organs on histology (*SI Appendix*, Fig. S8). Collectively, our results demonstrate that PTX/**1c**@ nanomicelles are safe and effective for use as theranostics to detect and treat cancer.

Conclusion

In this study, we have developed innovative self-assembling fluorinated dendrimer nanosystems for effective ^{19}F-MRI, ^{19}F-MRI-based multimodal imaging, and theranostics for cancer detection and treatment. Incorporating charged moieties adjacent to the fluorine moieties at the dendrimer terminals permitted fluorine nuclei mobility while retaining a high fluorine content with a good degree of water solubility. The resulting fluorinated nanosystem displayed favorable relaxation properties for effective ^{19}F-MRI. Importantly, the encapsulation of a pharmaceutical agent within the self-assembling supramolecular dendrimer core did not affect the relaxation properties of ^{19}F nuclei located on the surface of the nanoparticle; the two were sufficiently segregated in space to avoid interference.

Specifically, in this study, we used the fluorescence dye DiR and the anticancer drug PTX as model pharmaceutical agents to demonstrate the effectiveness of multimodal ^{19}F-MRI and NIRF imaging and theranostics achievable with our modular nanosystems for the simultaneous detection and treatment of cancer, in this case a pancreatic cancer patient-derived xenograft model. In particular, our nanosystems, whether PTX/DiR/**1c**@ or PTX/**1c**@, enabled effective and potent anticancer activity compared with PTX alone, which achieved no significant anticancer effect. This can be ascribed to the passive tumor targeting by PTX/DiR/**1c**@ and PTX/**1c**@ both exploiting the EPR effect unique to the tumor microenvironment for nanotechnology-based drug delivery.

The approach that we have demonstrated in this study can be readily adapted to the construction of modular nanosystems for the future personalized medicine, enabling targeted delivery of patient-specific pharmaceutical agents and imaging feedback of their effects. This concept of modular nanosystems issued from self-assembling supramolecular dendrimers has provided an innovative approach to creating a platform offering both imaging agents for various ^{19}F-MRI-based biomedical applications and multimodal theranostic agents for more efficient treatment and treatment monitoring. We are actively pursuing this direction.

Materials and Methods

Synthesis and Characterization of Dendrimers 1a-c. The synthetic protocols of **1a-c** are detailed in *SI Appendix*. **1a**: ^{1}H NMR (400 MHz, CD$_3$OD): δ 8.16 (s, 1H), 4.67 to 4.58 (m, 2H), 4.42 (t, J = 7.2 Hz, 2H), 4.32 (s, 2H), 3.29 to 3.16 (m, 4H), 2.95 to 2.57 (m, 8H), 1.96 to 1.86 (m, 2H), 1.40 to 1.23 (m, 30H), 0.90 (t, J = 6.8 Hz, 3H); ^{13}C NMR (101 MHz, CD$_3$OD/CDCl$_3$ = 1/1): δ 172.9, 170.5, 136.8, 126.2, 126.0 (q, J = 278.8 Hz), 53.4, 50.6, 46.7, 34.7 (q, J = 29.3 Hz), 31.8, 30.4, 30.3, 30.0, 29.6, 29.5, 29.4, 29.3, 29.22, 28.9, 26.4, 22.5, 13.9; ^{19}F NMR (376 MHz, CD$_3$OD): δ -65.65; HRMS: calcd. for $C_{35}H_{59}F_6N_6O_6^{+}$ [M+H]$^{+}$ 773.4400, found 773.4395. **1b**: ^{1}H NMR (400 MHz, CD$_3$OD): δ 8.17 (s, 1H), 4.54 to 4.45 (m, 4H), 4.40 (t, J = 7.1 Hz, 2H), 4.26 (s, 2H), 3.51 to 3.42 (m, 4H), 3.26 to 2.94 (m, 16H), 2.89 to 2.77 (m, 4H), 2.71 to 2.49 (m, 16H), 1.94 to 1.84 (m, 2H), 1.36 to 1.24 (m, 30H), 0.90 (t, J = 8.0 Hz, 3H); ^{13}C NMR (101 MHz, CD$_3$OD): δ 175.5, 175.3, 174.0, 172.6, 138.6, 127.9 (q, J = 277.8 Hz), 127.8, 53.8, 51.6, 51.4, 51.2, 50.4, 47.4, 36.3 (q, J = 28.3 Hz), 33.1, 31.3, 31.1, 30.8, 30.7, 30.6, 30.5, 30.2, 27.5, 23.7, 14.5; ^{19}F NMR (376 MHz, CD$_3$OD): δ -65.51; HRMS: calcd. for $C_{59}H_{96}N_{12}O_{14}F_{12}^{2+}$ [M+2H]$^{2+}$ 712.3483, found 712.3492. 1c: ^{1}H NMR (400 MHz, CD$_3$OD): δ 7.94 (s, 1H), 4.58 to 4.47 (m, 8H), 4.39 (t, J = 7.1 Hz, 2H), 3.82 (s, 2H), 3.31 – 3.21 (m, 12H), 2.89 to 2.72 (m, 36H), 2.67 to 2.53 (m, 20H), 2.50 to 2.30 (m, 28H), 1.95 to 1.83 (m, 2H), 1.34 to 1.24 (m, 30H), 0.90 (t, J = 6.6 Hz, 3H); ^{13}C NMR (151 MHz, CD$_3$OD/CDCl$_3$ = 1/1) δ 174.9, 174.8, 173.2, 172.6, 172.3, 172.2, 138.7, 127.2 (q, J = 277.8 Hz), 126.3, 53.3, 53.2, 53.0, 51.3, 50.8, 50.6, 50.0, 49.9, 49.7, 47.0, 37.8, 35.9 (q, J = 28.2 Hz), 35.4, 32.6, 31.5, 31.2, 31.1, 30.9, 30.3, 30.2, 30.1, 30.0, 29.7, 27.2, 23.3, 14.3; ^{19}F NMR (376 MHz, CD$_3$OD): δ -65.37; HRMS: calcd. for $C_{107}H_{169}F_{24}N_{24}O_{30}^{3+}$ [M+3H]$^{3+}$ 909.0689, found 909.0689.

^{19}F-MRI Studies. All MRI studies were carried out using a preclinical scanner operating at 7 T (Pharmascan 70/16 US Bruker BioSpin, Ettlingen, Germany) and a ^{1}H/^{19}F radiofrequency surface coil of 2 cm diameter. The experimental protocols are detailed in *SI Appendix*. In vitro relaxometry was performed to estimate longitudinal (T_1) and transverse (T_2) relaxation time constants of dendrimer solutions at 2.5 to 10 mM fluorine concentration followed by ^{19}F-MRI acquired with a voxel size of 2 × 2 × 2 mm^3 within <30 min. Using the same scanner and acquisition time, in vivo ^{19}F-MRI was acquired on ketamine/xylazine (100 mg kg^{-1}/10 mg kg^{-1}) anesthetized mice bearing L-IPC primary pancreatic cancer xenografts. In vivo imaging studies were approved by the local committee on ethics in animal research, authorized by the Ministry of Higher Education, Research and Innovation (project authorization no 30203), and conducted according to the EU Directive 2010/63/EU.

A full description of the *Materials and Methods* is provided in *SI Appendix, Materials and Methods*.

Data, Materials, and Software Availability. All study data are included in the article and *SI Appendix*.

ACKNOWLEDGMENTS. This work was supported by the Ligue Nationale Contre le Cancer (EL2016, EL2021 LNCCLiP, LP; doctoral fellowship grant, Z.L.), the French National Research Agency under the framework of the ERA-NET EURONANOMED European Research project "NAN-4-TUM" (L.P.), the EU H2020 Research and Innovation program NMBP "SAFE-N-MEDTECH" (2019 to 2023) (grant agreement No. 814607, B.R., T.R., Xiaoxuan Liu, L.P.), the EU Horizon Europe Research and Innovation program Cancer Mission "HIT-GLIO" (2023 to 2027) (grant agreement No. 101136835, L.P.), and China Scholarship Council (L.D. and X.L.). The relaxometric and preclinical MRI studies were performed at CRMBM, which is a member of France Life Imaging (grant ANR-11-INBS-0006 from the French "Investissements d'Avenir" program). E.L. and S.P. acknowledge financial support from the Italian Association for Cancer Research (AIRC, IG17413), and supercomputing resources from the ICSC – Centro Nazionale di Ricerca in High Performance Computing, Big Data, and Quantum Computing (Spoke 7, WP4 - Pilot applications, T.2.8 - Development and optimization of HPC-based integrated workflows based on flagship codes for personalized (nano)medicine), funded by the European Union – NextGenerationEU, and CINECA (Bologna, Italy).

Author affiliations: [a]Aix Marseille University, CNRS, Centre Interdisciplinaire de Nanoscience de Marseille (UMR 7325), Equipe Labellisée Ligue Contre le Cancer, Marseille 13288, France; [b]Aix Marseille University, CNRS, Institut de Chimie Radicalaire, UMR 7273, Marseille 13013, France; [c]Aix Marseille University, CNRS, Centre de Résonance Magnétique Biologique et Médicale, UMR 7339, Marseille 13385, France; [d]State Key Laboratory of Natural Medicines and Jiangsu Key Laboratory of Drug Discovery for Metabolic Diseases, Center of Drug Discovery, Center of Advanced Pharmaceuticals and Biomaterials, China Pharmaceutical University, Nanjing 211198, People's Republic of China; [e]Centre de Recherche en Cancérologie de Marseille, INSERM U1068, CNRS, UMR 7258, Institut Paoli-Calmettes, Aix Marseille Université, Marseille 13273, France; [f]Molecular Biology and Nanotechnology Laboratory, Department of Engineering and Architecture, University of Trieste, Trieste 34127, Italy; and [g]Department of General Biophysics, Faculty of Biology and Environmental Protection, University of Lodz, Lodz 90-236, Poland

Author contributions: L.P. conceived and coordinated the project; Z.L., T.-A.P.-B., A.V., Y.J., E.L., S.P., and L.P. designed research; Z.L., B.R., T.-A.P.-B., L.D., Y.J., B.L., T.R., Xi Liu, C.G., E.L., A.T., S.G., S.P., and A.V. performed research; Z.L., B.R., J.I., and M.B. contributed new reagents/analytic tools; Z.L., B.R., T.-A.P.-B., L.D., Y.J., B.L., Xi Liu, E.L., S.P., Xiaoxuan Liu, A.V., and L.P. analyzed data; and Z.L., B.R., T.-A.P.-B., L.D., B.L., Xi Liu, C.G., E.L., S.P., A.V., and L.P. wrote the paper.

1. M. G. Harisinghani, A. O'Shea, R. Weissleder, Advances in clinical MRI technology. *Sci. Transl. Med.* **11**, eaba2591 (2019).
2. E. Terreno, D. D. Castelli, A. Viale, S. Aime, Challenges for molecular magnetic resonance imaging. *Chem. Rev.* **110**, 3019–3042 (2010).
3. J. Wahsner, E. M. Gale, A. Rodriguez-Rodriguez, P. Caravan, Chemistry of MRI contrast agents: Current challenges and new frontiers. *Chem. Rev.* **119**, 957–1057 (2019).
4. I. Tirotta *et al.*, ^{19}F magnetic resonance imaging (MRI): From design of materials to clinical applications. *Chem. Rev.* **115**, 1106–1129 (2015).
5. D. Janasik, T. Krawczyk, ^{19}F MRI probes for multimodal imaging. *Chemistry* **28**, e202102556 (2022).
6. C. Zhang *et al.*, Biological utility of fluorinated compounds: From materials design to molecular imaging, therapeutics and environmental remediation. *Chem. Rev.* **122**, 167–208 (2022).
7. M. P. Krafft, J. G. Riess, Chemistry, physical chemistry, and uses of molecular fluorocarbon—Hydrocarbon diblocks, triblocks, and related compounds–Unique "apolar" components for self-assembled colloid and interface engineering. *Chem. Rev.* **109**, 1714–1792 (2009).
8. D. Jirak, A. Galisova, K. Kolouchova, D. Babuka, M. Hruby, Fluorine polymer probes for magnetic resonance imaging: Quo vadis? *MAGMA* **32**, 173–185 (2019).
9. Q. Peng *et al.*, Paramagnetic nanoemulsions with unified signals for sensitive ^{19}F MRI cell tracking. *Chem. Commun. (Camb.)* **54**, 6000–6003 (2018).
10. A. H. Jahromi *et al.*, Fluorous-soluble metal chelate for sensitive fluorine-19 magnetic resonance imaging nanoemulsion probes. *ACS Nano* **13**, 143–151 (2019).
11. A. H. Schmieder, S. D. Caruthers, J. Keupp, S. A. Wickline, G. M. Lanza, Recent advances in ^{19}Fluorine magnetic resonance imaging with perfluorocarbon emulsions. *Engineering (Beijing)* **1**, 475–489 (2015).
12. K. Wang, H. Peng, K. J. Thurecht, S. Puttick, A. K. Whittaker, Segmented highly branched copolymers: Rationally designed macromolecules for improved and tunable ^{19}F MRI. *Biomacromolecules* **16**, 2827–2839 (2015).
13. K. J. Thurecht *et al.*, Functional hyperbranched polymers: Toward targeted *in vivo* ^{19}F magnetic resonance imaging using designed macromolecules. *J. Am. Chem. Soc.* **132**, 5336–5337 (2010).
14. W. Du *et al.*, Amphiphilic hyperbranched fluoropolymers as nanoscopic ^{19}F magnetic resonance imaging agent assemblies. *Biomacromolecules* **9**, 2826–2833 (2008).
15. Z. Huang *et al.*, A fluorinated dendrimer-based nanotechnology platform new contrast agents for high field imaging. *Invest. Radiol.* **45**, 641–654 (2010).
16. X. Yue, M. B. Taraban, L. L. Hyland, Y. B. Yu, Avoiding steric congestion in dendrimer growth through proportionate branching: A twist on da Vinci's rule of tree branching. *J. Org. Chem.* **77**, 8879–8887 (2012).
17. W. Yu *et al.*, Design and synthesis of fluorinated dendrimers for sensitive 19F MRI. *J. Org. Chem.* **80**, 4443–4449 (2015).
18. J. M. Criscione *et al.*, Self-assembly of pH-responsive fluorinated dendrimer-based particulates for drug delivery and noninvasive imaging. *Biomaterials* **30**, 3946–3955 (2009).
19. M. Ogawa *et al.*, Synthesis and evaluation of water-soluble fluorinated dendritic block-copolymer nanoparticles as a 19F-MRI contrast agent. *Macromol. Chem. Phys.* **211**, 1602–1609 (2010).
20. X. Huang *et al.*, Multi-chromatic pH-activatable ^{19}F-MRI nanoprobes with binary ON/OFF pH transitions and chemical-shift barcodes. *Angew. Chem. Int. Ed. Engl.* **52**, 8074–8078 (2013).
21. S. E. Kirberger *et al.*, Synthesis of intrinsically disordered fluorinated peptides for modular design of high-signal ^{19}F MRI agents. *Angew. Chem. Int. Ed. Engl.* **56**, 6440–6444 (2017).
22. O. Munkhbat *et al.*, ^{19}F MRI of polymer nanogels aided by improved segmental mobility of embedded fluorine moieties. *Biomacromolecules* **20**, 790–800 (2019).
23. K. Wang *et al.*, pH-responsive star polymer nanoparticles: Potential ^{19}F MRI contrast agents for tumour-selective imaging. *Polymer Chem.* **4**, 4480–4489 (2013).
24. P. Garrigue *et al.*, Self-assembling supramolecular dendrimer nanosystem for PET imaging of tumors. *Proc. Natl. Acad. Sci. U.S.A.* **115**, 11454–11459 (2018).
25. L. Ding *et al.*, Bioimaging: Surface charge of supramolecular nanosystems for in vivo biodistribution: A MicroSPECT/CT imaging study (small 37/2020). *Small* **16**, 2070203 (2020).
26. L. Ding *et al.*, A self-assembling amphiphilic dendrimer nanotracer for SPECT imaging. *Chem. Commun.* **56**, 301–304 (2020).
27. L. Ding *et al.*, Modular self-assembling dendrimer nanosystems for magnetic resonance and multimodality imaging of tumors. *Adv. Mater.* **36**, e2308262 (2024), 10.1002/adma.202308262.
28. Y. Matsumura, H. Maeda, A new concept for macromolecular therapeutics in cancer chemotherapy: Mechanism of tumoritropic accumulation of proteins and the antitumor agent smancs. *Cancer Res.* **46**, 6387–6392 (1986).
29. L. E. Gerlowski, R. K. Jain, Microvascular permeability of normal and neoplastic tissues. *Microvasc. Res.* **31**, 288–305 (1986).

30. H. Maeda, Toward a full understanding of the EPR effect in primary and metastatic tumors as well as issues related to its heterogeneity. *Adv. Drug Deliv. Rev.* **91**, 3–6 (2015).
31. R. Sun *et al.*, The tumor EPR effect for cancer drug delivery: Current status, limitations, and alternatives. *Adv. Drug Deliv. Rev.* **191**, 114614 (2022).
32. V. Percec *et al.*, Self-assembly of Janus dendrimers into uniform dendrimersomes and other complex architectures. *Science* **328**, 1009–1014 (2010).
33. Z. Lyu, L. Ding, A. Tintaru, L. Peng, Self-assembling supramolecular dendrimers for biomedical applications: Lessons learned from poly(amidoamine) dendrimers. *Acc. Chem. Res.* **53**, 2936–2949 (2020).
34. J. Chen, D. Zhu, X. Liu, L. Peng, Amphiphilic dendrimer vectors for RNA delivery: State-of-the-art and future perspective. *Acc. Mater. Res.* **3**, 484–497 (2022).
35. T. Yu *et al.*, An amphiphilic dendrimer for effective delivery of small interfering RNA and gene silencing in vitro and in vivo. *Angew. Chem. Int. Ed. Engl.* **51**, 8478–8484 (2012).
36. D. Dhumal *et al.*, Dynamic self-assembling supramolecular dendrimer nanosystems as potent antibacterial candidates against drug-resistant bacteria and biofilms. *Nanoscale* **14**, 9286–9296 (2022).
37. E. Laurini *et al.*, "ITC for characterization of self-assembly process of cationic dendrons for siRNA delivery" in *Design and Delivery of SiRNA Therapeutics*, H. J. Ditzel, M. Tuttolomondo, S. Kauppinen, Eds. (Springer US, New York, NY, 2021), pp. 245–266.
38. M. Russi *et al.*, Some things old, new and borrowed: Delivery of dabrafenib and vemurafenib to melanoma cells via self-assembled nanomicelles based on an amphiphilic dendrimer. *Eur. J. Pharm. Sci.* **180**, 106311 (2023).
39. J. Kleeff *et al.*, Pancreatic cancer. *Nat. Rev. Dis. Primers* **2**, 16022 (2016).
40. E. S. Christenson, E. Jaffee, N. S. Azad, Current and emerging therapies for patients with advanced pancreatic ductal adenocarcinoma: A bright future. *Lancet Oncol.* **21**, e135–e145 (2020).
41. S. K. Garg, S. T. Chari, Early detection of pancreatic cancer. *Curr. Opin. Gastroenterol.* **36**, 456–461 (2020).
42. J. Liu *et al.*, Dendrimeric nanosystem consistently circumvents heterogeneous drug response and resistance in pancreatic cancer. *Exploration* **1**, 21–34 (2021).
43. A. N. Hosein, R. A. Brekken, A. Maitra, Pancreatic cancer stroma: An update on therapeutic targeting strategies. *Nat. Rev. Gastroenterol. Hepatol.* **17**, 487–505 (2020).
44. K. Wang *et al.*, Fluorescence image-guided tumour surgery. *Nat. Rev. Bioeng.* **1**, 161–179 (2023).
45. G. Hong, A. L. Antaris, H. Dai, Near-infrared fluorophores for biomedical imaging. *Nat. Biomed. Eng.* **1**, 0010 (2017).
46. P. J. Gawne, M. Ferreira, M. Papaluca, J. Grimm, P. Decuzzi, New opportunities and old challenges in the clinical translation of nanotheranostics. *Nat. Rev. Mater.* **8**, 783–798 (2023).
47. H. Chen, W. Zhang, G. Zhu, J. Xie, X. Chen, Rethinking cancer nanotheranostics. *Nat. Rev. Mater.* **2**, 17024 (2017).
48. Y. Jiang *et al.*, Dendrimer nanosystems for adaptive tumor-assisted drug delivery via extracellular vesicle hijacking. *Proc. Natl. Acad. Sci. U.S.A.* **120**, e2215308120 (2023).
49. T. Wei *et al.*, Anticancer drug nanomicelles formed by self-assembling amphiphilic dendrimer to combat cancer drug resistance. *Proc. Natl. Acad. Sci. U.S.A.* **112**, 2978–2983 (2015).